

RESEARCH ARTICLE | AUGUST 23 2023

# A human ear-inspired ultrasonic transducer (HEUT) for 3D localization of sub-wavelength scatterers



Special Collection: [Fundamentals and Applications of Metamaterials: Breaking the Limits](#)

Luzhen Nie ; Matthieu Toulemonde ; Meng-Xing Tang ; Steven Freear ; Sevan Harput

Check for updates

*Appl. Phys. Lett.* 123, 082203 (2023)

<https://doi.org/10.1063/5.0152029>



View Online



Export Citation

CrossMark

## Articles You May Be Interested In

Instrumental speech-quality measures: New insights, ideas, and results

*J Acoust Soc Am* (February 1999)

Human ear-inspired ultrasonic transducers able to locate objects in three dimensions

*Scilight* (August 2023)

Frequency and amplitude estimation of the first peak of head-related transfer functions from individual pinna anthropometry

*J. Acoust. Soc. Am.* (February 2015)

### 500 kHz or 8.5 GHz? And all the ranges in between.

Lock-in Amplifiers for your periodic signal measurements



Find out more



# A human ear-inspired ultrasonic transducer (HEUT) for 3D localization of sub-wavelength scatterers



Cite as: Appl. Phys. Lett. **123**, 082203 (2023); doi: [10.1063/5.0152029](https://doi.org/10.1063/5.0152029)

Submitted: 27 March 2023 · Accepted: 28 July 2023 ·

Published Online: 23 August 2023







View Online



Export Citation



CrossMark

Luzhen Nie,<sup>1</sup>  Matthieu Toulemonde,<sup>2</sup>  Meng-Xing Tang,<sup>2</sup>  Steven Freear,<sup>1</sup>  and Sevan Harput<sup>3,a)</sup> 

## AFFILIATIONS

<sup>1</sup>School of Electronic and Electrical Engineering, University of Leeds, Leeds, United Kingdom

<sup>2</sup>Department of Bioengineering, Imperial College London, London, United Kingdom

<sup>3</sup>Division of Electrical and Electronic Engineering, London South Bank University, London, United Kingdom

**Note:** This paper is part of the APL Special Collection on Fundamentals and Applications of Metamaterials: Breaking the Limits.

<sup>a)</sup>Author to whom correspondence should be addressed: [harputs@lsbu.ac.uk](mailto:harputs@lsbu.ac.uk)

## ABSTRACT

The proposed technology aims to enable 3D localization of scatterers using single element ultrasonic transducers, which are traditionally limited to 1D measurements. This is achieved by designing a bespoke acoustic lens with a spiral-shaped pattern similar to the human outer ear, a shape that has evolved for sound source localization. This lens breaks the surface symmetry of the transducer, allowing ultrasonic waves arriving from different directions to be encoded in a certain way that can later be decoded to extract directional information. By employing the mechanism of spatial-encoding of the received signals and decoding via signal processing, the location of sub-wavelength scatterers can be detected in 3D with a single measurement for sparsely distributed scatterers. The proposed technology is first verified through a simulation study, and then 3D printed acoustic lenses are used to demonstrate the 3D encoding functionality of the Human Ear-inspired Ultrasonic Transducer (HEUT) experimentally. A framework is created to localize scatterers in 3D by processing received signals acquired by a HEUT prototype. With this technology, a single transducer can obtain multi-dimensional information with a single pulse-echo measurement, reducing the number of elements required for performing 3D ultrasound localization. The proposed spatial-encoding and -decoding technology can be applied to other wave-based imaging methods to develop affordable, practical, and compact sensing devices.

Published under an exclusive license by AIP Publishing. <https://doi.org/10.1063/5.0152029>

Simpler, more affordable, compact, and energy-efficient 3D acoustic localization systems are desired for use in a wide range of nondestructive testing (NDT) and underwater search and survey applications, such as autonomous underwater vehicles (AUVs) and handheld sonar devices.<sup>1–3</sup> However, the implementation of such a 3D system typically employs either multiple elements/channels or multiple measurements with cumbersome mechanical rotating units to acquire 3D information,<sup>4–8</sup> resulting in high hardware complexity, cost, and dimensions. In this study, an acoustic lens is designed to enable spatial-encoding of the received signal, which can achieve 3D underwater localization with a single measurement performed by a single element ultrasound transducer without any moving parts, promising a hardware efficient system that could find applications in NDT, AUVs, and handheld sonar devices.

Conventionally, 3D localization is not possible by only using a single element ultrasound transducer. Consider three scenarios, where a scatterer is relocated with the identical radial distance ( $r$ ) but different polar ( $\theta$ ) and azimuthal ( $\varphi$ ) angles, as schematically illustrated in

**Fig. 1.** By definition, the A-mode method only uses the envelope of the received signal to find the radial distance of the scatterer through a time-of-flight measurement. Therefore, A-mode scans performed for all three scenarios will result in the same 1D information, radial distance. Although the envelopes of the signals are almost the same, there are considerable differences between the received echoes in scenario 1 and 2 or scenario 1 and 3, as shown in Fig. 1. The differences are due to the spatial filtering effect of the transducer, which modifies the received echo depending on the angle of incidence. By using the phase of the signal as explained in Ref. 9, scatterers can be localized in 2D, ( $r, \theta$ ), where scenario 1 and 2 or scenario 1 and 3 can be differentiated, but it is not possible to differentiate scenario 2 from scenario 3 as the received signal is identical for both cases. However, when the transducer surface symmetry is broken, the ultrasound waves arriving from different azimuthal directions will be distorted in a distinct manner.

To break the surface symmetry and achieve 3D localization, we developed an ultrasound transducer with an acoustic lens inspired by the human ear. The asymmetry of the human outer ear, pinna, plays

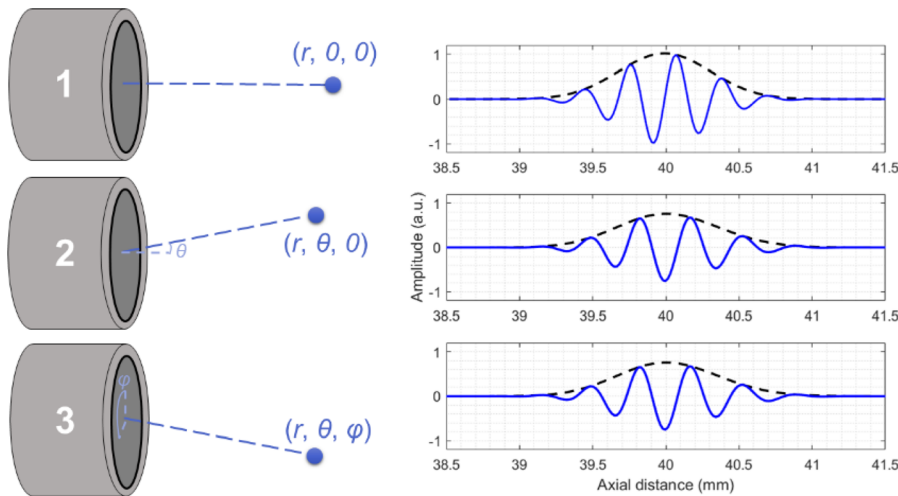


**FIG. 1.** Three different scenarios are schematically illustrated to highlight the importance of breaking the surface symmetry. (Left) Illustration of the transducer and scatterer positions. For each scenario, the scatterer is relocated to different spherical coordinates with respect to the center of the transducer. (Right) The received signals and their envelopes are shown in blue and dashed black lines, respectively. It is not possible to differentiate between scenario 2 and 3, since the transducer's aperture is symmetric, and a relocation of the scatterer with different azimuths ( $\varphi$ ) does not change the received signal.

an essential role for localization in hearing.<sup>10</sup> Researchers have shown that the pinna performs a location-dependent filtering of sounds, providing spectral cues that help to determine the direction of a sound source.<sup>11</sup> While most humans rely on both the shape of the pinna and the differential information provided by two ears for sound source localization, monaural listeners are able to localize sound source elevation and azimuth based on spectral cues alone.<sup>12</sup> To replicate this spatial filtering capability of the pinna, we considered implementing different features of the outer ear, such as helix, antihelix, concha, tragus, and lobule. However, Guezenoc and Segquier demonstrated that helix and antihelix are the main components of the human ear based on their principle component analysis of a wide dataset of human ear shapes.<sup>13</sup> Similarly, Chen and Bhanu showed that the helix and antihelix are the most significant features of the outer ear used for 3D ear recognition.<sup>14</sup> By using this phenomenon, we propose a Human Ear-inspired Ultrasonic Transducer (HEUT) in this study, which is based on the helix and antihelix of the pinna to improve the localization capability of single element transducers. With a single acquisition, HEUT can identify the locations of sub-wavelength scatterers in 3D.

For the acoustic lens design, the helix and antihelix features of the outer ear were implemented by a spiral-shaped mask to break the transducer surface symmetry. The spiral-shaped mask in a form of air filled channels was embedded in a 3D printed lens, which was then

attached to a single element ultrasound transducer to form a HEUT prototype, as shown in Fig. 2.

The helix was first designed with a single spiral, and a second spiral was added to implement the antihelix feature (see Fig. 2, top-left). A single element transducer of 6-mm diameter working at 2.4 MHz was chosen for both simulations and experiments. Both the thickness of the spirals and the separation angle between the two spirals were designed by using Field II,<sup>15,16</sup> and the values of a quarter of the wavelength and 90° were adopted. During transmission, the acoustic lens had a negligible effect on the transmit beam profile in the far field. During reception, the dual spiral-shaped mask encoded the received signal in a certain way that was possible to decode and extract directional information. Field II utilizes the Tupholme–Stepanishen method<sup>15</sup> to simulate linear ultrasound transducer fields and ultrasound pulse echo. It solves the simulation analytically, defining the transducer aperture with rigid-baffle boundary conditions. In addition to the transducer's shape and aperture size, it requires the definitions of the excitation signal, electromechanical pulse response, and scatterer locations along with their intensities. In the simulations, a one-cycle sinusoid at 2.4 MHz was adopted as the excitation signal, and a Gaussian pulse with a center frequency of 2.4 MHz and a 60% fractional bandwidth was used as the electromechanical pulse response. Arbitrary units were used in both the simulations and the presentation

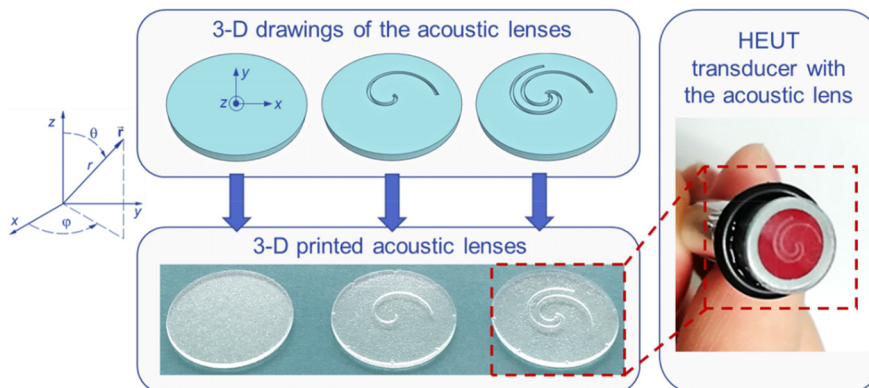


**FIG. 2.** (Top-left) 3D drawing of the acoustic lenses with no mask (empty lens) and a single spiral- and dual spiral-shaped mask. (Bottom-left) Photograph of the 3D printed acoustic lenses. (Right) Photograph of the HEUT prototype transducer with an acoustic lens. The coordinate systems are shown on the left for clarity.

20 September 2023 14:42:57

of simulation results. Further details about the acoustic lens design and simulations are explained in the supplementary material. Please refer to the statement at the end of the manuscript for code availability.

The lenses were then additively manufactured with a Form 3L SLA printer (Formlabs, MA, USA) with ELEGOO ABS-like photopolymer resin. A solid cylinder block of 0.6 mm thickness and 9.6 mm diameter was made as the empty lens for reference. The designed lenses had the identical cylinder shape but with single or dual spiral-shaped grooves (air channels) on one side to create the surface asymmetry as shown in Fig. 2. The air channels had a width and depth of 250  $\mu\text{m}$ , corresponding to  $\lambda/4$  at a frequency of 2.4 MHz for a sound speed of 2400 m/s through the lens material. The acoustic attenuation of the lens material was measured to be 11.4 dB/cm/MHz at 2.4 MHz, and the density was 1.2 g/cm<sup>3</sup>, resulting in an acoustic impedance of 2.88 MPa s/m. In experiments, acoustic lenses were placed in contact with the transducer to block part of the transducer's active surface using spiral-shaped masks with acoustically opaque air channels.

The ultrasound setup consisted of a single element transducer working at 2.4 MHz (Olympus Scientific Solutions Americas Inc., MA), acoustic lenses, and an Ultrasound Array Research Platform (UARP),<sup>17–19</sup> which was used to measure directional responses (spatial-encoding) of the acoustic lenses. A 200- $\mu\text{m}$  wire was used as the point scatterer. A one-cycle sinusoid at 2.4 MHz was used as the transmit waveform. The transducer was moved by a motorized translation stage (MTS50C-Z8, Thorlabs Ltd., UK). More details of the experimental setup are provided in the supplementary material.

Simulations were first performed to compare the performance of a control measurement without a mask, and measurements with a single spiral- and dual spiral-shaped mask. Figure 3(a) shows the received signals from seven different scatterers located at the following spherical  $(r, \theta, \varphi)$  coordinates;  $r = 40$  mm and  $\varphi = 90^\circ$  with a varying polar angle of  $\theta = 0^\circ, 0.72^\circ, 1.43^\circ, 2.15^\circ, 2.87^\circ, 3.58^\circ$ , and  $4.3^\circ$ . These locations corresponded to lateral translation of a scatterer in the x-direction as  $x = 0, 0.5, 1.0, 1.5, 2.0, 2.5$ , and  $3.0$  mm (see Fig. 2 or Fig. S1 in the supplementary material for axes). The purpose of this simulation was to show that the spiral-shaped masks can be used to detect the polar angle of the scatterer,  $\theta$ .<sup>9</sup>

Figure 3(a) (right column) shows the spatial-encoding of the received signal as a result of lateral translation of the scatterer, which effectively changes with the angle of incidence,  $\theta$ . For all three simulations with or without a mask, the spectral peak shifts as a function of the scatterer angle,  $\theta$ . For the dual spiral-shaped mask, the angle  $\theta$  of the scatterer could be determined with Eq. (1), where  $f_p$  is the frequency peak in MHz and  $\theta$  is the polar angle of the scatterer in degrees,

$$f_p = 2.331 - 0.009\theta^2. \quad (1)$$

Equation (1) was formulated by fitting a polynomial to the peak frequency response, and it can be used to estimate the polar angle with an average error of  $0.04^\circ$  and a maximum error of  $0.19^\circ$ , which was validated for  $0^\circ \leq \theta \leq 5^\circ$  and  $0^\circ \leq \varphi < 360^\circ$  with simulations.

To reproduce the problem described in Fig. 1, another simulation was performed with two mirrored scatterers located at the following spherical  $(r, \theta, \varphi)$  coordinates: (40.1 mm,  $4.05^\circ, 135^\circ$ ) and (40.1 mm,  $4.05^\circ, 315^\circ$ ), which corresponded to (2, -2, 40) and (-2, 2, 40) mm in x-y-z coordinates. Figure 3(b) shows the received signals from these

scatterers, where the empty mask cannot achieve 3D encoding as the mirrored scatterers located at (2, -2, 40) and (-2, 2, 40) mm provide the identical signal due to the symmetrical aperture of the transducer.

Both the single spiral- and dual spiral-shaped masks break this symmetry and could be used to differentiate these scatterers. The azimuthal angle of the scatterer could be determined by finding the zero-crossing of the signal's phase shown in Fig. 3(b) (right bottom for the dual spiral-shaped mask), where the phase response of the scatterer located at  $\varphi = 135^\circ$  has a zero-crossing at 2.35 MHz and for  $\varphi = 315^\circ$ , it is 2.56 MHz. The zero-crossing point could be used to unambiguously locate the scatterers since it changes with the azimuthal angle as verified in simulations. For the dual spiral-shaped mask, the azimuthal angle of the scatterer could be determined with Eq. (2), where  $f_{zc}$  is the zero-crossing frequency of the signal's phase in MHz and  $\varphi$  is the angle in degrees,

$$f_{zc} = 2.35 + 9 \times 10^{-6}(\varphi - 125)^2. \quad (2)$$

Equation (2) can be used to estimate the azimuthal angle with an average and maximum error of  $11.1^\circ$  and  $17.2^\circ$ , as validated for the simulations performed at  $\theta = 4.05^\circ$  and  $0^\circ \leq \varphi < 360^\circ$ .

In another simulation, the localization capability of the dual spiral-shaped mask was further tested using 25 random scatterers with a uniform distribution. These scatterers were within the main transmit beam, between 15 and 50 mm in the z-direction and up to 3 mm away from the main axis in the x- and y-directions.

A localization framework consisting of three steps was developed to determine the location of scatterers in spherical coordinates.

1. Measure the time of flight of the received signal to calculate  $r$ . This approach is the same as the A-mode scan.
2. Measure the location of the received signal's spectral peak to estimate  $\theta$  using an equation similar to Eq. (1), which is recalculated at each axial depth.
3. Measure the zero-crossing point of the received signal's phase response to estimate  $\varphi$  using an equation similar to Eq. (2), which is recalculated at each axial depth.

The reason for recalculating Eqs. (1) and (2) is due to the attenuation, where the quadratic part of the equations stayed the same but the offset frequency changed by depth.

The localization errors for the 25 randomly distributed scatterers generated within the x-y-z Cartesian coordinates of (-3:3, -3:3, 15:50) mm were calculated, where the error was the Euclidian distance between the correct and predicted 3D positions. Figure 4 shows the corresponding localization errors for each randomly distributed scatterer, which is  $0.30 \pm 0.36$  mm for HEUT with the dual spiral-shaped mask, compared to  $1.81 \pm 0.90$  mm for a traditional A-scan mode.

First set of experimental measurements were performed to verify the simulations presented in Fig. 3(a) using a point scatterer placed at (0, 0, 40) mm. The transducer was then moved along the x-direction with a distance up to 3 mm at increments of 0.5 mm, where Fig. 5(a) shows the corresponding results. Note that the radial distance is changing between 40 and 40.22 mm due to the limitation of the translation stage.

The spatial filtering effect of the single element transducer is observable in Fig. 5(a), where the received pressure field varies in both the time and frequency domains for a scatterer at different lateral locations. As shown in Fig. 5(a), 2D localization could be unambiguously

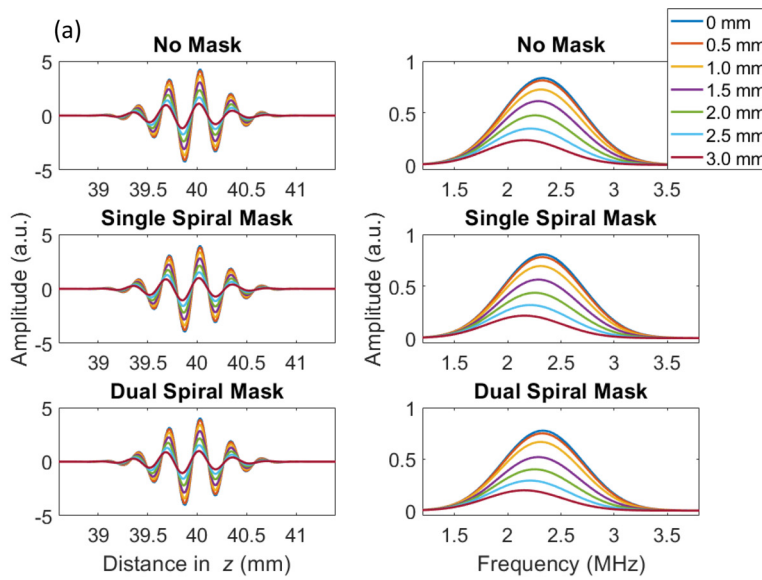


FIG. 3. (a) (Left) Time domain signals for seven simulated scatterers, (right) corresponding spectral amplitudes of the received signals for an empty lens, and lenses with a single spiral- and dual spiral-shaped mask. (b) Time and frequency domain comparison of the simulated received signals for scatterers located at  $(2, -2, 40)$  and  $(-2, 2, 40)$  mm for an empty lens, and lenses with a single spiral- and dual spiral-shaped mask.

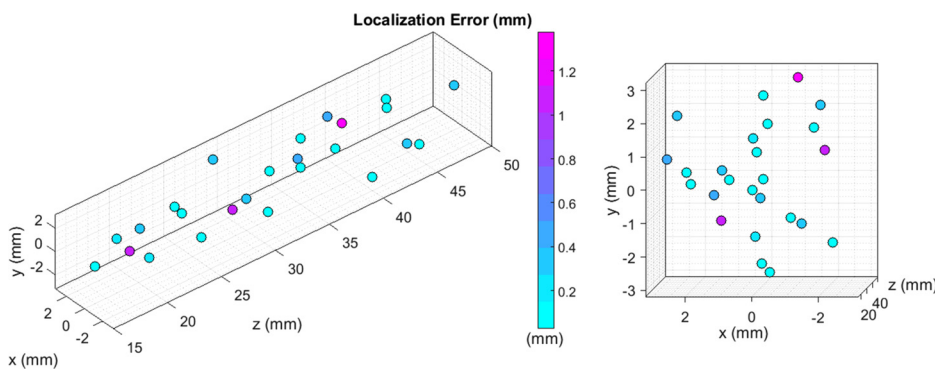
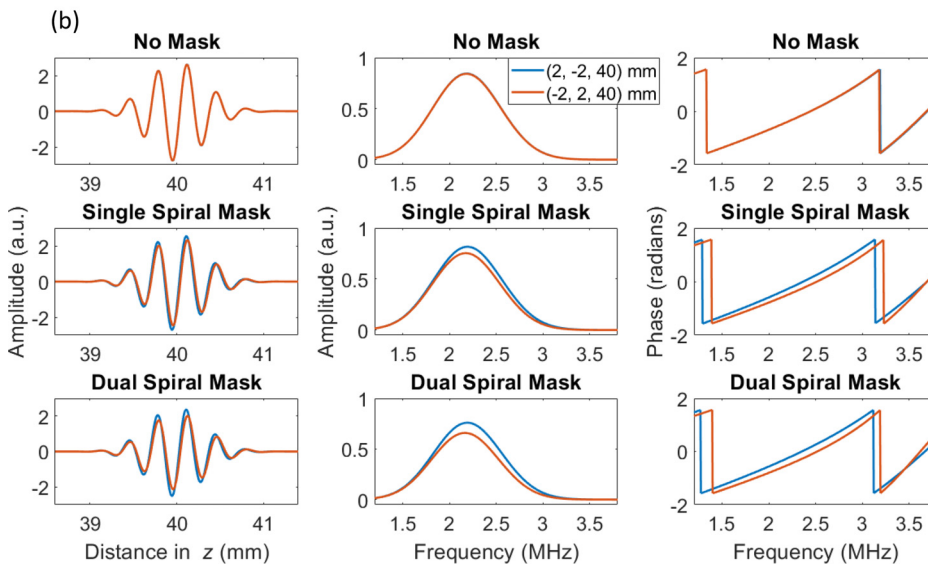


FIG. 4. Localization errors for 25 randomly simulated scatterers within the  $x$ - $y$ - $z$  Cartesian coordinates of  $(-3:3, -3:3, 15:50)$  mm. Left and right figures are the same scatterers plotted from different viewing angles for better visualization. Each scatterer is plotted at their exact location and color-coded according to their 3D localization error.

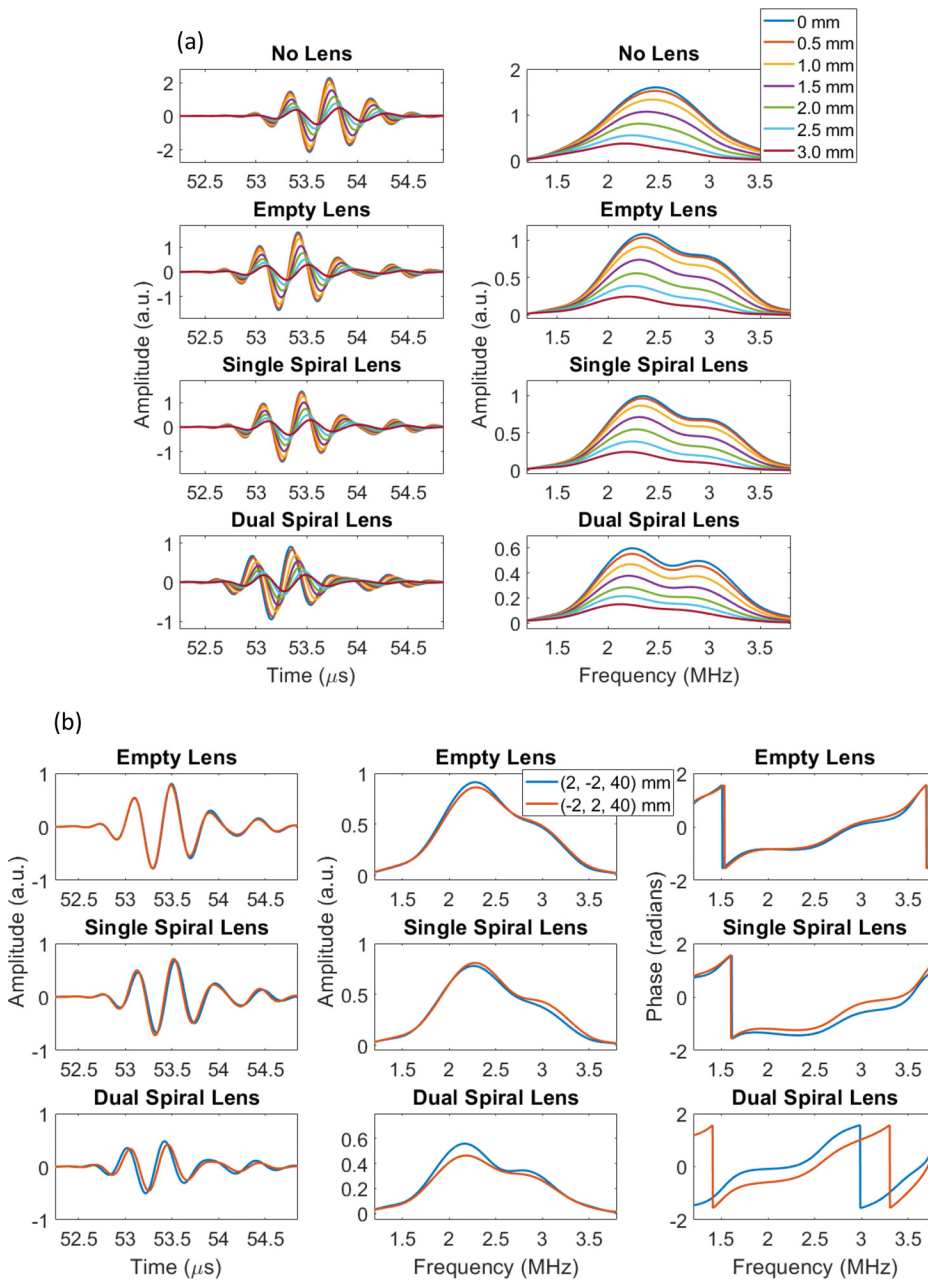


FIG. 5. (a) Received echoes for seven scatterers located at varying lateral locations are shown (left) in the time domain with corresponding (right) spectral amplitudes. (b) Time and frequency domain comparison of the received signals from scatterers located at (2, −2, 40) and (−2, 2, 40) mm for an empty lens and lenses with a single spiral- and dual spiral-shaped mask.

performed by finding the shift in the frequency domain, similar to the simulation study as shown in Fig. 3(a). The angular detection equation now becomes the following due to experimental nuances:

$$f_p = 2.239 - 0.006\theta^2. \tag{3}$$

Equation (3) could be used to estimate the polar angle with an average error of 0.25° and an outlier error value of 0.89°.

When the lenses are placed in front of the transducer, the received waveforms in the time domain have tails due to reverberations within the lens as shown in Fig. 5(a) (left column). Correspondingly, a secondary peak at around 3 MHz is seen in Fig.

5(a) (right column). This is one of the main differences between the simulations and experiments, where an ideal lens can be implemented in simulations without generating any reverberations. However, the proposed method can identify the location of a sub-wavelength scatterer even in the presence of reverberations.

Second set of experimental measurements were performed with scatterers located at (2, −2, 40) mm and (−2, 2, 40) mm in order to demonstrate the functionality of the acoustic lens to solve the 3D localization problem described in Fig. 1 and simulated in Fig. 3(b). Figure 5(b) shows the temporal waveforms, their corresponding spectra, and phase responses for measurements acquired using an empty lens and

lenses with a single spiral- and dual spiral-shaped mask. The measurements with an empty lens are provided as control, which cannot achieve 3D encoding as expected, where the received signals from mirrored scatterers are almost identical. The surface symmetry is not strongly broken with a single spiral-shaped lens in simulations, and additional experimental imperfections make the separation of these two mirrored scatterers difficult with this lens. In contrast, the lens with a dual spiral-shaped mask introduces more phase diversity, leading to a more effective encoding. The azimuthal angle of the scatterer, for the lens with a dual spiral-shaped mask, could be determined by finding the zero-crossing of the signal's phase shown in Fig. 5(b) (right bottom), where the phase response of the scatterer located at  $\varphi = 135^\circ$  has a zero-crossing at 2.25 MHz, and for  $\varphi = 315^\circ$ , it is 2.52 MHz. The azimuthal angles of these two scatterers could be estimated with an error of  $13.5^\circ$  through a modified version of Eq. (2), where the frequency offset is changed to 2.25 due to experimental nuances.

In this work, we adapted the helix and antihelix shape of the pinna to design an acoustic lens with a spiral-shaped mask, resulting in a spatial filter that was sensitive not only to changes in the polar angle of  $\theta$  but also to the azimuthal angle of  $\varphi$ . This technology can localize smaller-than-wavelength scatterers when their echoes can be separated in the time domain. This proof-of-concept study validated the working principle of the HEUT prototype by combining a single element ultrasound transducer and bespoke acoustic lenses. The designed dual spiral mask achieved a 3D localization accuracy better than half a wavelength (0.31 mm for 2.4 MHz in water) on average for a set of randomly distributed scatterers *in silico*. Experiments showed that it is possible to identify the scatterer location in 3D, though decoding of the received signal is not a straightforward task. The decoding of the polar and azimuthal angles could be performed by using empirical formulas, which need re-calibration for each specific transducer and acoustic lens pair. In addition, the measurement hardware could also affect the decoding process, and a re-calibration may be required. The burden of the calibration process could be eased with several ways, and the easiest way could be the generation of a self-calibration method or the design of an adaptive filter to compensate for variations in transducer-lens response. If the proposed method is widely adopted, then manufacturers can perform the calibration of their transducers with the acoustic lenses. Empirical formulas have been investigated as one of the possible ways to decode the polar and azimuthal angles for localization in 3D. In the future work, the 3D localization process could be automated by using artificial intelligence-based solutions, such as training a neural network that incorporates the transducer-to-transducer variations,<sup>20,21</sup> attenuation,<sup>22</sup> multiple scattering,<sup>22</sup> and phase aberrations.<sup>23,24</sup>

A circular single element ultrasound transducer of 6 mm diameter has been chosen in the current study, and the used frequency of 2.4 MHz is within the range of multi-beam forward-looking sonar systems.<sup>2</sup> These values are chosen for illustrative purposes in this proof-of-concept study and would vary depending on practical requirements. For a given single element ultrasound transducer, it is possible to determine its radiating beam pattern either analytically or numerically. The proposed method in this study is designed to operate within the far field of the transducer, where the beam profile is relatively uniform and well-behaved with limited amplitude and phase irregularities. For the circular single element transducer used in the current study, its

near field length and beam divergence can be analytically calculated.<sup>25</sup> The beam divergence refers to the angle between one side of the beam and the central axis in the far field, where the transducer works more efficiently within this range. The localization range (or maximum detectable polar angle) achievable with the proposed method is constrained by the beam divergence, not by the design of the acoustic lens. For specific applications, it is possible to increase the beam divergence and, consequently, the localization range (or maximum detectable polar angle) by employing different means. This includes using a transducer with a smaller aperture size<sup>25</sup> or incorporating an additional divergent acoustic lens.

The HEUT technology does not require complex hardware, expensive electronics, or moving parts, since the decoding of the direction information is performed in software using data acquired from a single channel. With a single element ultrasonic transducer, the proposed HEUT technology can be immediately applied for the detection of small defects in homogeneous materials or the localization of scatterers in hypo-echoic mediums. This technology can also be applied to handheld sonar devices and other wave-based imaging methods, such as Radar or Terahertz imaging. This technology can be a starting point to develop affordable, practical, and compact sensing devices for new scientific applications.

See the supplementary material for the bioinspiration and numerical simulations of the lens design and the setup for experimental measurements.

This work was funded by the Royal Society under Grant No. RGS\R1\201012 and the U.K. EPSRC under Grant No. EP/P023266/1.

## AUTHOR DECLARATIONS

### Conflict of Interest

The authors have no conflicts to disclose.

### Author Contributions

**Luzhen Nie:** Conceptualization (equal); Data curation (equal); Formal analysis (equal); Investigation (lead); Methodology (lead); Resources (equal); Software (equal); Validation (equal); Visualization (equal); Writing – original draft (lead); Writing – review & editing (equal). **Matthieu Toulemonde:** Investigation (supporting); Methodology (supporting); Writing – review & editing (equal). **Meng-Xing Tang:** Investigation (supporting); Methodology (supporting); Supervision (supporting); Writing – review & editing (equal). **Steven Freear:** Investigation (supporting); Methodology (supporting); Supervision (supporting); Writing – review & editing (equal). **Sevan Harput:** Conceptualization (lead); Data curation (equal); Formal analysis (equal); Funding acquisition (lead); Methodology (supporting); Project administration (lead); Resources (equal); Validation (equal); Visualization (equal); Writing – original draft (lead); Writing – review & editing (equal).

## DATA AVAILABILITY

The data that support the findings of this study are available from the corresponding author upon reasonable request.

## REFERENCES

- <sup>1</sup>A. Sahoo, S. K. Dwivedy, and P. S. Robi, "Advancements in the field of autonomous underwater vehicle," *Ocean Eng.* **181**, 145–160 (2019).
- <sup>2</sup>Y. Wei, Y. Duan, and D. An, "Monitoring fish using imaging sonar: Capacity, challenges and future perspective," *Fish Fish.* **23**(6), 1347–1370 (2022).
- <sup>3</sup>S. Karabchevsky, K. David, O. Ben-Harush *et al.*, "FPGA-based adaptive speckle suppression filter for underwater imaging sonar," *IEEE J. Oceanic Eng.* **36**(4), 646–657 (2011).
- <sup>4</sup>R. P. Hodges, *Underwater Acoustics: Analysis, Design and Performance of Sonar* (John Wiley & Sons, 2011).
- <sup>5</sup>Z. Lin, Y. Chen, X. Liu *et al.*, "Optimized design for sparse arrays in 3-D imaging sonar systems based on perturbed Bayesian compressive sensing," *IEEE Sensors J.* **20**(10), 5554–5565 (2020).
- <sup>6</sup>P. Kruizinga, P. van der Meulen, A. Fedjajevs *et al.*, "Compressive 3-d ultrasound imaging using a single sensor," *Sci. Adv.* **3**(12), e1701423 (2017).
- <sup>7</sup>P. van der Meulen, P. Kruizinga, J. G. Bosch *et al.*, "Coding mask design for single sensor ultrasound imaging," *IEEE Trans. Comput. Imaging* **6**, 358–373 (2020).
- <sup>8</sup>J. Janjic, P. Kruizinga, P. Van Der Meulen *et al.*, "Structured ultrasound microscopy," *Appl. Phys. Lett.* **112**(25), 251901 (2018).
- <sup>9</sup>L. Nie, J. T. M. Moo, M. Toulemonde *et al.*, "Localization of a scatterer in 3D with a single measurement and single element transducer," in *IEEE International Ultrasonics Symposium (IUS)* (IEEE, 2020), pp. 1–4.
- <sup>10</sup>D. W. Batteau, "The role of the pinna in human localization," *Proc. R. Soc. London, Ser. B* **168**, 158–180 (1967).
- <sup>11</sup>V. Best and S. Carlile, "The role of high frequencies in speech localization," *J. Acoust. Soc. Am.* **118**, 353–363 (2005).
- <sup>12</sup>M. M. Van Wanrooij and A. J. V. Opstal, "Contribution of head shadow and pinna cues to chronic monaural sound localization," *J. Neurosci.* **24**(17), 4163–4171 (2004).
- <sup>13</sup>C. Guezenc and R. Segquier, "A wide dataset of ear shapes and pinna-related transfer functions generated by random ear drawings," *J. Acoust. Soc. Am.* **147**(6), 4087–4096 (2020).
- <sup>14</sup>H. Chen and B. Bhanu, "Human ear recognition in 3D," *IEEE Trans. Pattern Anal. Mach. Intell.* **29**(4), 718–737 (2007).
- <sup>15</sup>J. A. Jensen and N. B. Svendsen, "Calculation of pressure fields from arbitrarily shaped apodized and excited ultrasound transducers," *IEEE Trans. Ultrason., Ferroelectr., Freq. Control* **39**(2), 262–267 (1992).
- <sup>16</sup>J. A. Jensen, "Field: A program for simulating ultrasound systems," in *Paper presented at the 10th Nordic-Baltic Conference on Biomedical Imaging* (Medical & Biological Engineering & Computing, 1996), Vol. 4, pp. 351–353.
- <sup>17</sup>P. R. Smith, D. M. J. Cowell, B. Raiton *et al.*, "Ultrasound array transmitter architecture with high timing resolution using embedded phase-locked loops," *IEEE Trans. Ultrason., Ferroelectr., Freq. Control* **59**(1), 40–49 (2012).
- <sup>18</sup>D. M. J. Cowell, P. R. Smith, and S. Freear, "Phase-inversion-based selective harmonic elimination (PI-SHE) in multi-level switched-mode tone- and frequency-modulated excitation," *IEEE Trans. Ultrason., Ferroelectr., Freq. Control* **60**(6), 1084–1097 (2013).
- <sup>19</sup>P. R. Smith, D. M. J. Cowell, and S. Freear, "Width-modulated squarewave pulses for ultrasound applications," *IEEE Trans. Ultrason., Ferroelectr., Freq. Control* **60**(11), 2244–2256 (2013).
- <sup>20</sup>Y. Zhang, X. He, Z. Tian *et al.*, "Multi-needle detection in 3D ultrasound images using unsupervised order-graph regularized sparse dictionary learning," *IEEE Trans. Med. Imaging* **39**(7), 2302–2315 (2020).
- <sup>21</sup>R. J. van Sloun, O. Solomon, M. Bruce *et al.*, "Super-resolution ultrasound localization microscopy through deep learning," *IEEE Trans. Med. Imaging* **40**(3), 829–839 (2021).
- <sup>22</sup>N. Blanken, J. M. Wolterink, H. Delingette *et al.*, "Super-resolved microbubble localization in single-channel ultrasound RF signals using deep learning," *IEEE Trans. Med. Imaging* **41**(9), 2532–2542 (2022).
- <sup>23</sup>D. Saha, U. Schmidt, Q. Zhang *et al.*, "Practical sensorless aberration estimation for 3D microscopy with deep learning," *Opt. Express* **28**, 29044–29053 (2020).
- <sup>24</sup>S. Jeon, W. Choi, B. Park *et al.*, "A deep learning-based model that reduces speed of sound aberrations for improved *in vivo* photoacoustic imaging," *IEEE Trans. Image Process.* **30**, 8773–8784 (2021).
- <sup>25</sup>D. A. Christensen, *Ultrasonic Bioinstrumentation* (John Wiley & Sons, 1988).